




Dark mode enhancing magneto-optical Kerr effect in multilayer magnetoplasmonic crystalsA. Yu. Frolov ^{1,*}, M. R. Shcherbakov ^{1,2} and A. A. Fedyanin ¹¹*Faculty of Physics, Lomonosov Moscow State University, Moscow 119991, Russia*²*School of Applied and Engineering Physics, Cornell University, Ithaca, New York 14853, USA*

(Received 7 March 2019; revised manuscript received 6 December 2019; published 8 January 2020)

Magnetic materials in metallic nanostructures allow an external magnetic field to easily control surface plasmon polaritons and surface lattice modes (SLMs), which enhances the value of magneto-optical response. The present paper demonstrates both experimentally and numerically that the inherently different radiative damping of dark and bright SLMs in one-dimensional low-loss multilayer Au/Ni/Au magnetoplasmonic crystals can alter the resonant enhancement of the transverse magneto-optical Kerr effect (TMOKE). As the quality factor of dark SLMs goes up, the maximum TMOKE values increase as well. The spectral range of TMOKE enhancement broadens at small incident angles since dark and bright SLMs overlap each other. The Fano resonance model shows that the wavelength shift of the dark and bright modes results in the resonant enhancement of TMOKE.

DOI: [10.1103/PhysRevB.101.045409](https://doi.org/10.1103/PhysRevB.101.045409)**I. INTRODUCTION**

Surface plasmon polaritons (SPPs) are coupled oscillations of free electrons and light that are strongly localized at a metal/dielectric interface [1]. Two important features of SPPs—evanescent field and long propagation length—have been successfully applied to plasmonic circuits and chips [2]. Further development of plasmonic devices requires means of active modulation of SPP propagation. A merger between plasmonics and magneto-optics, known as magnetoplasmonics, promotes active modulation of SPPs [3] and spectacularly expands functionalities of plasmonic nanostructures [4,5]. One of the simplest and most efficient ways to excite SPPs is to use plasmonic crystals, i.e., one- or two-dimensional periodically nanostructured metal surfaces. Plasmonic crystals in combination with the magnetic material, called magnetoplasmonic crystals (MPCs), significantly enhance the magneto-optical effects as compared to the bulk magnetic materials [6–9] and thin plasmonic films [10,11]. For instance, transverse magneto-optical Kerr effect (TMOKE) may increase by one order of magnitude in all-ferromagnetic MPCs supporting highly damped SPP modes [6,7]. Depending on the absorption and radiative losses, the SPP quality factor regulates the enhancement of magneto-optical effects. To decrease the inherent SPP absorption losses, noble metals and magnetic dielectrics have been implemented to magnetoplasmonic systems [12–18].

To reduce the radiative damping in magnetoplasmonic nanostructures, the broadband plasmons were hybridized in the array of gold nanowires using a spectrally narrow waveguide mode in a thin magnetic film; as a result, the quality factor of such hybrid modes increased and Faraday rotation was enhanced [19]. Being ordered in one- or two-dimensional arrays, the radiative damping of localized surface plasmons

(LSPs) in metal nanoparticles gets significantly suppressed. If diffraction orders propagate along the array, LSPs in nanoparticles can couple to each other. These diffractively coupled LSPs form collective surface lattice modes (SLMs) characterized by an extremely narrow Fano line shape and a high Q factor [20]. The polar magneto-optical Kerr effect is resonantly enhanced by the excitation of SLMs in a rectangular array of nickel nanodisks; this process can be spectrally controlled by tuning the lattice periodicity [21]. The tunability of polar magneto-optical Kerr effect induced by SLMs can be significantly expanded if a disk-shaped unit cell is modified to an elliptical nickel nanoantenna [22].

The phenomenon of LSPs coupling in different diffraction orders provides the excitation of bright and dark modes with a different radiative damping [23]. The resonant enhancement of magneto-optical effects induced by different SLMs seems to be the process that should deserve careful attention. Regarding the radiative losses, the localized and propagating dark surface plasmon modes have a considerable advantage over the bright modes: they increase the sensitivity of plasmonic sensors [24–26], the lasing of dye molecules [27], and the value of magneto-optical effects [28]. As opposed to bright modes with strong dipole activity, dark modes exhibit zero net dipole moment because of an antisymmetric field distribution. Therefore, dark modes demonstrate strongly suppressed radiative damping, longer lifetime, and propagation length. To circumvent the weak coupling of dark optical modes to incident radiation the symmetry of the system should be broken by an oblique light incidence or a localized source should be used near plasmonic or all-dielectric single nanoparticles, dimers, trimers, chains, and more complex structures [24,29–32]. One-dimensional (1D) plasmonic crystals with narrow slits support the excitation of both bright and dark SPP modes which results from hybridization of two different order SPPs. This hybridization may take place in a narrow angle range and a spectral one of the incident light [33]. It should be noted that the use of a 1D array of gold nanowires [34] or

*frolov@nanolab.phys.msu.ru

a 2D gold array of nanoantennas [23,35] allows SLMs to be excited within an wide spectral range by changing an incident angle.

The present work shows that the difference in the radiative damping of bright and dark SLMs can be regarded as an additional way to control magneto-optical effects. More specifically, we have studied the efficiency of the magneto-optical response in magnetoplasmonic crystals made of low-loss multilayer Au/Ni/Au nanowires. The angular-wavelength measurements of transmittance revealed the excitation of the dark and bright SLMs in the one-dimensional MPC due to the diffractive coupling of $\lambda-$ (antisymmetric) and $3\lambda/2-$ (symmetric) order LSPs supported by individual multilayer Au/Ni/Au nanowires. The angular-wavelength measurements of TMOKE revealed that TMOKE enhancement values resulting from the excitation of dark SLMs are higher compared to those of bright SLMs. The magnetization-induced wavelength shifts of both dark and bright SLMs were analytically estimated using the Fano resonance model, which showed that the wavelength shifts of the dark and bright modes contributed to the resonant enhancement of TMOKE. This MPC can promote further advances in magnetoplasmonic nanostructures designed for light modulation, sensing [36,37], SPP controlling in nanophotonic devices [38] as well as in plasmonic and all-dielectric magneto-optical active nanoantennas [22,39–41], ultrafast SPP-induced dynamics of magneto-optical effects [42–44], and magnetic recording [45].

II. RESULTS AND DISCUSSION

A. Experimental sample and setup

Three metallic layers, Au(100 nm)/Ni(10 nm)/Au(10 nm), were deposited on an optically transparent sapphire (Al_2O_3) substrate by a magnetron sputtering technique. The array of nanowires were fabricated by perforating the Au/Ni/Au film with focused ion beam. The total area of the sample was $100 \times 100 \mu\text{m}^2$. Figure 1(a) demonstrates a scanning electron microscope (SEM) image of the MPC surface (period is $d = 430 \text{ nm}$; width of slits is $w = 60 \text{ nm}$). The SEM image in Fig. 1(b) shows a tilted view of the MPC cut made by focused ion beam. The fabricated nanowires of Au/Ni/Au MPC have a trapezoid profile with the base angle of 70° [Fig. 1(c)]. The angular-wavelength dependence of the transmittance is used to reveal the excitation of LSPs and SLMs in MPCs. The experimental setup for measuring TMOKE and transmittance spectra depending on the incident angle is shown in Fig. 2. A halogen lamp (HL) with a monochromator (M) was used as a source of light for the spectral measurements in the visible and near-infrared ranges. The polarization of incoming light was oriented perpendicularly to nanowires of the MPC. The collimated light beam was focused by an objective (O1) with a numerical aperture of $\text{NA} = 0.15$ into a spot with a diameter of $100 \mu\text{m}$ at the MPC plane. The sample was mounted on an xyz translating holder. The transmitted light was collected by the second objective (O2), NA = 0.37, and delivered to a photomultiplier tube (PMT) through a multimode optical fiber. The lock-in detection technique with a chopper (Ch) modulating the light intensity at the frequency of 117 Hz was utilized to measure the transmittance $T(0)$ without any ex-

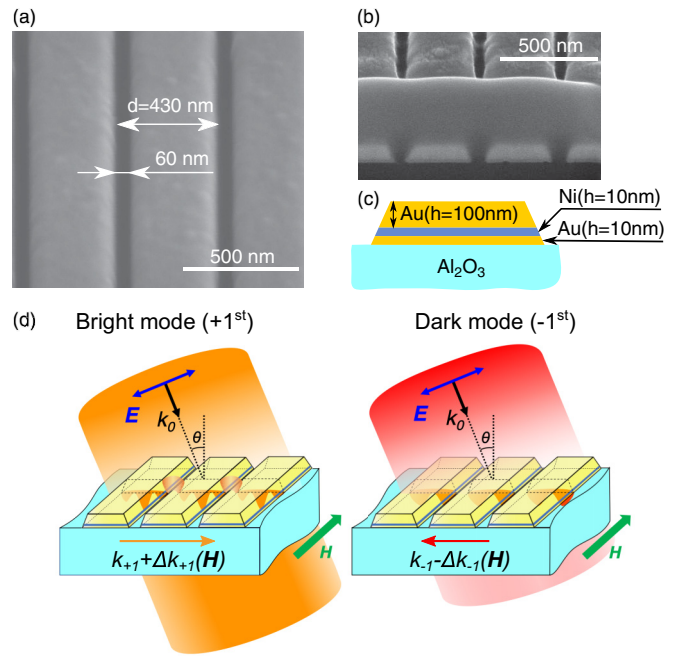


FIG. 1. (a) Scanning electron microscope (SEM) image representing the surface of Au/Ni/Au multilayer nanowires of MPC. (b) Tilted view SEM image of MPC slice. (c) Profile of a single MPC nanowire. (d) The scheme of excitation of bright and dark modes in MPC. $\Delta k_{\pm 1}$ shows the changes of SLMs wave vectors ($k_{\pm 1}$) caused by an external transverse magnetic field \mathbf{H} .

ternal magnetic field. The MPC was magnetized by applying an alternating magnetic field (\mathbf{H}) to the transverse plane at a frequency of 86 Hz and an amplitude of 16 mT, which led to a modulation of the transmittance $\Delta T = T(\mathbf{H}) - T(-\mathbf{H})$. The TMOKE was defined as $\delta = \Delta T/T(0)$.

B. Localized surface plasmons in individual Au/Ni/Au nanowires

The existence of the LSPs in the individual Au/Ni/Au nanowire on a sapphire substrate is revealed by simulations of angular-wavelength cross-section extinction [Fig. 3(a), $\sigma_{\text{ext}} = \sigma_{\text{abs}} + \sigma_{\text{scat}}$] and field distribution [Fig. 3(b)] (see more information in the Supplemental Material [46], Sec. I). TM polarized light was incident on the individual nanowire from above. The extinction peak around $\lambda = 605 \text{ nm}$ appeared to be almost independent of the wavelength within the incident angle from $\theta = 0^\circ$ to $\theta = 20^\circ$. $|E_x|$ near-field and E_x phase at

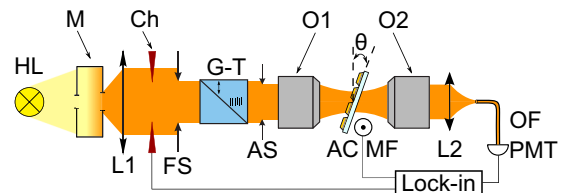


FIG. 2. The scheme of TMOKE and transmittance spectra measurements of Au/Ni/Au MPC. Halogen lamp (HL); objectives (O1, O2); lenses (L1, L2); optical chopper (Ch); Lock-in amplifier; optical fiber (OF); photomultiplier tube (PMT).

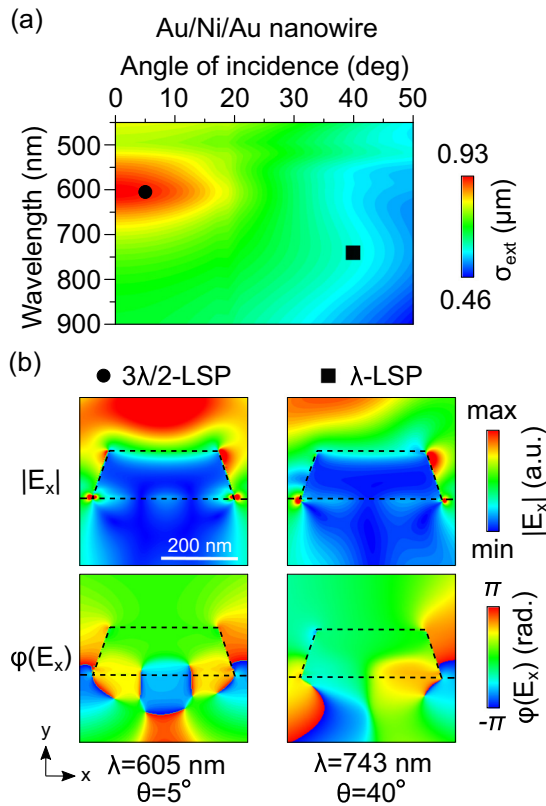


FIG. 3. (a) Simulated cross-section extinction of the individual infinite Au/Ni/Au nanowire on the Al_2O_3 substrate. (b) $|E_x|$ and phase $\varphi(E_x)$ of $3\lambda/2$ - and λ -order LSPs in the individual nanowire.

$\lambda = 605$ nm and $\theta = 5^\circ$ [Fig. 3(b)] possess three E_x antinodes associated with the excitation of the $3\lambda/2$ -order LSP (symmetric mode). The second extinction peak appeared around $\lambda = 743$ nm at high incident angles from $\theta = 30^\circ$ to $\theta = 50^\circ$. The $|E_x|$ near-field and E_x phase distribution at $\lambda = 743$ nm and $\theta = 40^\circ$ shows the mode with two E_x antinodes. This antisymmetric field distribution is associated with the λ -order LSP.

C. Angular-wavelength transmittance spectra

The bright and dark SLMs in the MPC result from the diffractive coupling of $3\lambda/2$ - and λ -order LSPs, supported by an individual infinite Au/Ni/Au nanowire with a trapezoid cross section. LSPs and SLMs in Au/Ni/Au MPC were revealed by measurements and simulations of angular-wavelength transmittance spectra. Figures 4(a) and 4(b) show the experimental and simulated angular-wavelength transmittance of the MPC within an angle range from $\theta = -12^\circ$ to $\theta = 20^\circ$ and within a wavelength range from $\lambda = 450$ nm to $\lambda = 900$ nm. The simulation of MPC transmittance [Fig. 4(b)] was performed using a finite-difference time-domain solver (Lumerical FDTD Solutions [47]) taking into account the numerical aperture of the collecting objective. Experimental and simulated spectra were demonstrated to agree with each other. In the transmittance spectra, a broad shoulder at $\lambda = 620$ nm was observed at all angles owing to the excitation of LSP in individual nanowires of MPC [see the black solid curve in Figs. 4(a) and 4(b)]. The $|E_x|$ near-field distribution

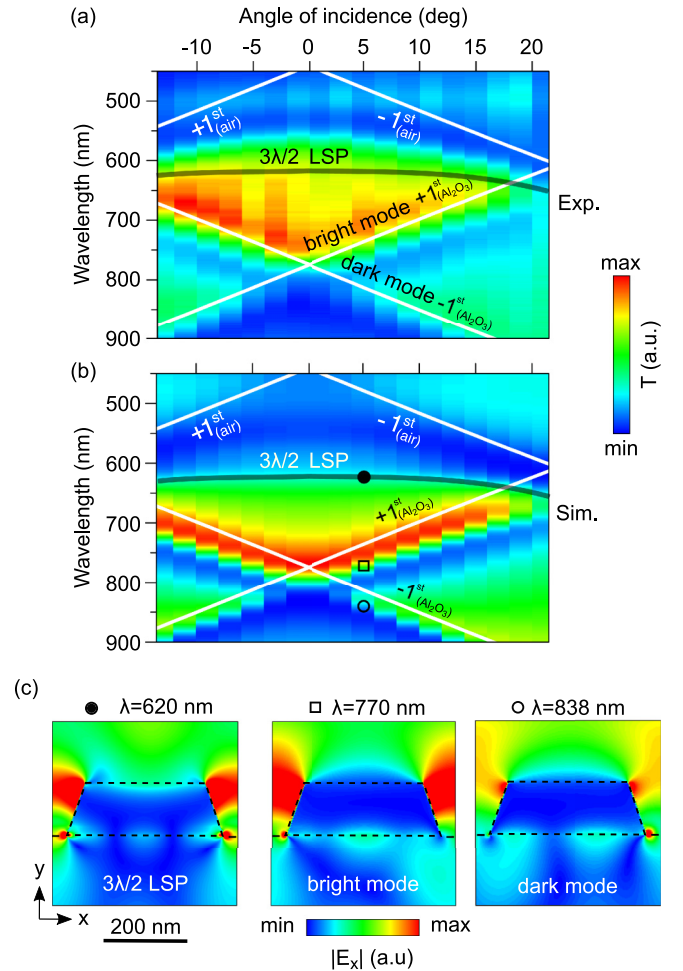


FIG. 4. The angular-wavelength transmittance of the MPC: (a) experimental, (b) FDTD simulation. The solid white curves present RA dispersion laws. (c) $|E_x|$ distribution of LSP, bright and dark modes, respectively, calculated for $\theta = 5^\circ$. Spectral positions of electric-field distribution are shown on the angular-wavelength transmittance (b) using the open square and the circle. (d) Simulated transmittance (black curve) and spectral dependence of electric-field intensity σ integrated over Ni layer (blue curve) of the MPC. The angle of the light incidence is $\theta = 5^\circ$. Three dashed color curves indicate Lorentz lines, with quality factors of 9.9, 9.4, and 30, respectively, corresponding to σ (cyan solid curve).

of the LSP at $\theta = 5^\circ$ is shown in Fig. 4(c) (black circle). Three antinodes located at the Au/ Al_2O_3 interface reveal the $3\lambda/2$ -order LSP with a nonzero in-plane electric dipole moment. This distribution is similar to the one observed for the

individual nanowire at $\lambda = 605$ nm. When the $\pm 1^{st}$ diffraction orders appear in the MPC plane, i.e., in the case of a Rayleigh anomaly (RA), LSPs are coupled to each other by means of diffraction and form $\pm 1^{st}$ SLMs. The calculated RAs that were obtained with the diffraction orders disappearing at the Al_2O_3 interface $\lambda_R^{(\text{Al}_2\text{O}_3)} = d[n_{\text{Al}_2\text{O}_3} \pm \sin \theta]$ and at the air interface $\lambda_R^{(\text{air})} = d[1 \pm \sin \theta]$ are shown with white solid curves in Figs. 4(a) and 4(b). The dispersion laws of $\pm 1^{st}$ RAs lie on the two angle-dependent transmittance maxima of both experimental and simulated spectra [Figs. 4(a) and 4(b)]. In addition to the maxima, well-pronounced angle-dependent minima of transmittance are observed at the wavelength that is longer than that of RAs. The asymmetric line shape of transmittance arises from Fano interference between LSPs and diffraction orders. The difference of the transmittance value at the $\pm 1^{st}$ SLMs is associated with the one of the near-field distribution of the $\pm 1^{st}$ SLMs. Figure 4(c) shows the simulated distribution of the $|E_x|$ of $\pm 1^{st}$ SLMs at $\theta = 5^\circ$ (open square and circle). The $+1^{st}$ SLM excited at $\lambda = 770$ nm has three antinodes (symmetric mode) located at the Al_2O_3 interface and, therefore, possesses a nonzero in-plane dipole moment. The $|E_x|$ distribution of the $+1^{st}$ SLM coincides with the $3\lambda/2$ -order LSP in the individual nanowire. The $|E_x|$ distribution of the -1^{st} SLM at $\lambda = 838$ nm has two antinodes (antisymmetric mode), resulting in a near-zero dipole moment. The $|E_x|$ distribution of the -1^{st} SLM coincides with the λ -order LSP in the individual nanowire excited at high incidence angles [see Fig. 3(b)]. The excitation and coupling of the λ -order LSP at small angles in the MPC is possible owing to the -1^{st} diffraction order which propagates at the Al_2O_3 interface. The diffraction order is analogous to the incident light at high angles. The excitation of this mode is forbidden at the normal illumination coming from the far field. Figure S1 of the Supplemental Material [46] shows that the phase signs of the neighboring $|E_x|$ antinodes are opposite each other for the $\pm 1^{st}$ SLMs. It appeared that the dipole activity resulting in smaller values of transmittance peaks near RAs was lower for the dark mode than for the bright one. At that, the electric field in the slits of MPC turned out to be significantly smaller in the antisymmetric mode as compared to the symmetric one.

In order to estimate the quality factor of LSPs and SLMs in the MPC, we simulated the spectral dependence of the electric-field localization inside the Ni layer. Figure 4(d) shows the way the electric-field energy concentrated in the Ni layer $\sigma = \iint |E|^2 dS$ (blue solid curve) and transmittance (black solid curve) at $\theta = 5^\circ$ depend on the wavelength. The quality factors of LSPs, bright, and dark modes are calculated by decomposition of the electric-field energy spectrum to three Lorentz-shape curves (see dashed color curves). The first maximum of σ spectrum at $\lambda = 620$ nm is associated with the electric-field enhancement of the $3\lambda/2$ -order LSP with $Q = 9.9$. The other two σ maxima at $\lambda = 770$ nm and $\lambda = 838$ nm are associated with the resonant electric field of the bright and dark SLMs. The dark SLM possesses a narrower full width at half maximum of σ ($\Gamma_{-1} = 0.075 \times 10^{15} \text{ s}^{-1}$) compared to the bright one ($\Gamma_{+1} = 0.256 \times 10^{15} \text{ s}^{-1}$). The quality factor of the dark SLM is larger than that of the bright SLM (30 and 9.4, respectively). To figure out the influence of the excitation of propagating SPPs, the SPP wavelength

was compared to the maximum of electric-field localization (see the Supplemental Material [46], ‘‘Comparison of SLM and SPP wavelengths’’ section). A large mismatch of the SPP wavelength and electric-field localization maximum shows that coupling of the incident light with SPP is weak and SLMs are dominant modes in the MPC under scrutiny.

D. Transverse magneto-optical Kerr effect

Figure 5 shows the experimental transmittance spectra (black curves) observed at angles of the light incidence θ in the range from $\theta = 0^\circ$ to $\theta = 20^\circ$. The excitation of dark SLMs ($\lambda > 800$ nm) results in smaller transmittance peaks compared to those of symmetric SLMs ($\lambda < 800$ nm). The experimental TMOKE spectra (red square dots) are also shown in Fig. 5. First, at $\theta = 0^\circ$ [Fig. 5(a)], TMOKE is close to zero. A small TMOKE signal is provoked by a slightly focused incident light beam. An increase in the incident angle broadens the spectral distance between bright and dark SLMs. At $\theta = 20^\circ$ [Fig. 5(f)], a single resonance of TMOKE appears due to the excitation of bright SLM. It has two local maxima with $\delta_{\text{max}} = \pm 0.1\%$. The spectral position of the TMOKE maximum corresponds to the slope of the transmittance resonance, where ΔT reaches its maximum as well. When the angle of incidence decreases, the dark SLM contributes to TMOKE resonant behavior. The opposite propagation direction of dark and bright SLMs results in the opposite spectral shift of the transmittance in the external magnetic field. At $\theta = 5, 10^\circ$ [Figs. 5(c) and 5(d)] and $\lambda \approx 800$ nm the negative part of the TMOKE resonance induced by the bright SLM overlaps with the negative part of the dark one. Therefore, when the bright and dark SLMs’ spectral positions are close one to each other, the TMOKE enhancement wavelength ranges overlap and broaden compared to the excitation of a single SLM. The TMOKE maximum value associated with the excitation of dark and bright SLM is equal to $\delta_{\text{max}} = -0.27\%$ at $\lambda = 835$ nm and $\delta_{\text{max}} = 0.1\%$ at $\lambda = 770$ nm, respectively [Figs. 5(c) and 5(d)]. In contrast, the average TMOKE value within the nonresonant wavelength ranges from $\lambda = 640$ nm to $\lambda = 660$ nm at $\theta = 5^\circ$ is significantly smaller and is equal to $\delta_{\text{nonres}} = 0.002\%$. The comparison of TMOKE at the maximum points and in the nonresonant case gives the TMOKE enhancement of $\delta_{\text{max}}/\delta_{\text{nonres}} = 135$ and $\delta_{\text{max}}/\delta_{\text{nonres}} = 50$ at the excitation of dark and bright SLMs, respectively. Thus, the TMOKE enhancement induced by dark SLMs is almost three times higher than the one induced by bright SLMs. The field of both SLMs penetrates to the Ni layer. Transverse magnetization of the Ni layer induces nondiagonal components ($\epsilon_{yz}^{\text{Ni}}$) in the permittivity tensor. The propagation of SLMs at the $\text{Au}/\text{Al}_2\text{O}_3$ interface is modified, likewise to SPPs in MPCs [4,6,9,17,18]. SLM wave vectors change their values (Δk_{SLM}), which in their turn leads to the spectral shifting, to the broadening of Fano resonances, and a strong enhancement of TMOKE.

E. Influence of the wavelength shift of SLM on TMOKE

The Fano resonance model is applied to show the influence that the wavelength shift produces on TMOKE. The transmittance spectra of the MPC with and without a magnetic

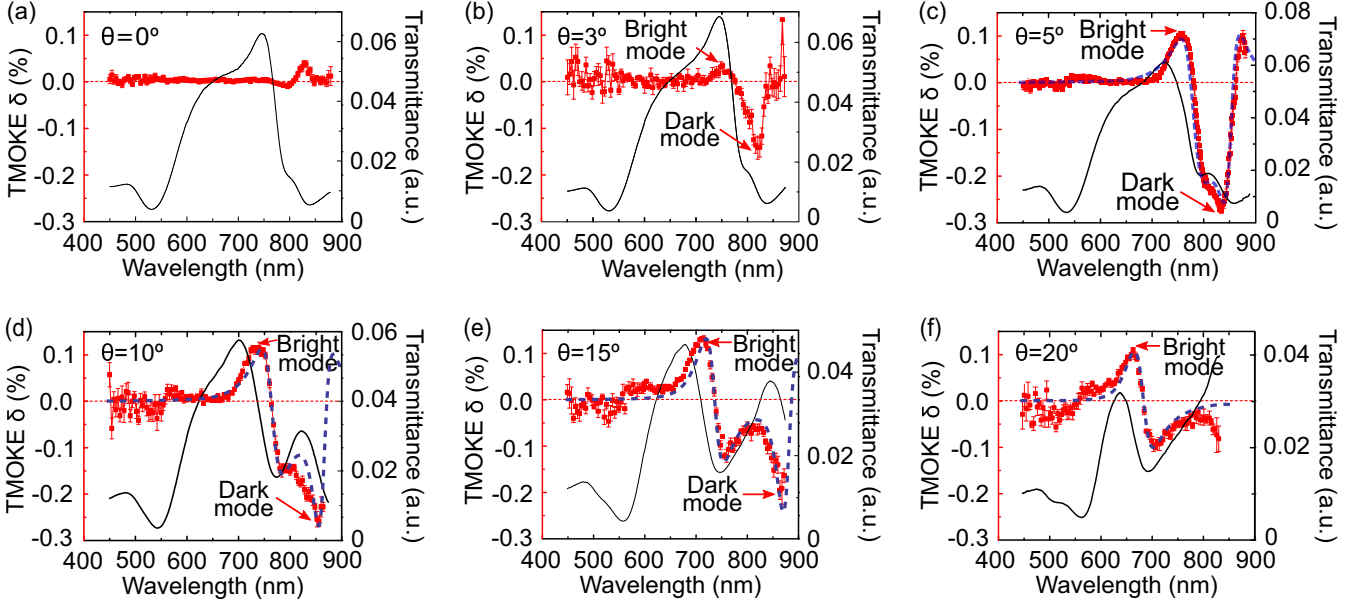


FIG. 5. Angular spectra of TMOKE (red squares) and transmittance spectra (black curves) of Au/Ni/Au MPC. Panels (a)–(f) correspond to various incident angles. Dashed curves stand for the calculated TMOKE.

field and TMOKE were calculated using two Fano resonances of $\pm 1^{st}$ SLMs with different damping [33], and broad LSP radiation:

$$T(\omega, 0) = \left| A + \frac{b_{+1}\Gamma_{+1}e^{i\phi_{+1}}}{\omega - \omega_{+1} + i\Gamma_{+1}} + \frac{b_{-1}\Gamma_{-1}e^{i\phi_{-1}}}{\omega - \omega_{-1} + i\Gamma_{-1}} \right|^2 + \frac{b_0^2\Gamma_0^2}{(\omega - \omega_0)^2 + \Gamma_0^2}, \quad (1)$$

$$T(\omega, \mathbf{H}) = \left| A + \frac{b_{+1}\Gamma_{+1}e^{i\phi_{+1}}}{\omega - \omega_{+1} + \Delta\omega_{+1} + i\Gamma_{+1}} + \frac{b_{-1}\Gamma_{-1}e^{i\phi_{-1}}}{\omega - \omega_{-1} - \Delta\omega_{-1} + i\Gamma_{-1}} \right|^2 + \frac{b_0^2\Gamma_0^2}{(\omega - \omega_0)^2 + \Gamma_0^2}, \quad (2)$$

$$\delta_{\text{theory}} = \frac{T(\omega, \mathbf{H}) - T(\omega, 0)}{T(\omega, 0)}, \quad (3)$$

where ω is the frequency of light, $\omega_{0,\pm 1}$ and $b_{0,\pm 1}$ are $3\lambda/2$ -order LSP and $\pm 1^{st}$ SLM frequencies and amplitudes, respectively, $\phi_{\pm 1}$ is the phase retardation of the SLM scattered light with respect to the nonresonant transmitted light, A is the amplitude of nonresonant transmitted light; $\Gamma_0, \Gamma_{\pm 1}$ are the sum of Ohmic and radiative losses of $3\lambda/2$ -order LSPs and $\pm 1^{st}$ SLMs, respectively; $\Delta\omega_{\pm 1}$

is the magnetization-induced shift of the $\pm 1^{st}$ SLM frequencies. The result of calculated TMOKE at $\theta = 5\text{--}20^\circ$ incident angles is shown in Figs. 5(c)–5(f) (dashed curves) along with the experimental results. All the fitting parameters are listed in Table I. $\Gamma_{\pm 1}$ values ($\Gamma_{-1} = 0.077 \times 10^{15} \text{ s}^{-1} < \Gamma_{+1} = 0.2 \times 10^{15} \text{ s}^{-1}$) are approximately the same as those obtained from σ . The calculated frequency shift is approximately the same for both bright and dark modes. The frequency (wavelength) shift is equal to $\Delta\omega_{-1} = 0.1 \times 10^{12} \text{ s}^{-1}$ ($\Delta\lambda_{-1} = 2\pi c\Delta\omega_{-1}/\omega_{-1}^2 = 0.0385 \text{ nm}$) for the dark mode and $\Delta\omega_{+1} = 0.115 \times 10^{12} \text{ s}^{-1}$ ($\Delta\lambda_{+1} = 0.0389 \text{ nm}$) for the bright mode. However, compared to the bright mode, the lower damping of the dark mode results in a greater TMOKE enhancement.

III. CONCLUSIONS

The present research reveals that a one-dimensional magnetoplasmonic crystal consisting of multilayer (Au/Ni/Au) nanowires promotes an efficient control of surface lattice modes (SLMs) by means of an external magnetic field. The angular dependence of TMOKE shows that the spectral range of TMOKE enhancement is tunable owing to the bright ($+1^{st}$) and dark (-1^{st}) SLMs resulting from the diffractive coupling of $3\lambda/2$ - and λ -order LSPs. It is shown that the

TABLE I. Parameters of Fano resonance model at $\theta = 5\text{--}20^\circ$.

θ (deg)	A	ω_0 (10^{15} s^{-1})	ω_{+1} (10^{15} s^{-1})	ω_{-1} (10^{15} s^{-1})	b_0	b_{+1}	b_{-1}	Γ_0 (10^{15} s^{-1})	Γ_{+1} (10^{15} s^{-1})	Γ_{-1} (10^{15} s^{-1})	ϕ_{+1} (rad)	ϕ_{-1} (rad)	$\Delta\omega_{+1}$ (10^{15} s^{-1})	$\Delta\omega_{-1}$ (10^{15} s^{-1})
5	0.180	2.98	2.360	2.215	0.15	0.157	0.081	0.256	0.19	0.077	-2.121	-0.561	0.000115	0.00010
10	0.215	2.98	2.430	2.191	0.15	0.187	0.120	0.256	0.20	0.077	-1.901	-0.561	0.000115	0.00010
15	0.225	2.98	2.580	2.161	0.15	0.205	0.120	0.256	0.20	0.077	-1.501	-0.561	0.000115	0.00010
20	0.182	2.98	2.720	1.950	0.15	0.205	0.120	0.256	0.20	0.077	-1.301	-0.561	0.000130	0.00010

dark mode largely suppresses radiative damping and results in the TMOKE value being almost three times higher than that at the bright mode. Compared to the TMOKE at the nonresonant spectral range, the observed enhancement factor equals 135 for the dark mode and 50 for the bright mode. The Fano resonance model showed that the magnetization-induced wavelength shift of SLMs is the key factor for the TMOKE enhancement in the MPC. Thus, engineering and modeling electromagnetic modes and their quality factors is a promising way to design efficient magneto-optical materials.

ACKNOWLEDGMENTS

Authors acknowledge financial support from Ministry of Science and Higher Education of the Russian Federation Contract No. 14.W03.31.0008 (sample fabrication); Russian Foundation for Basic Research Contracts No. 17-52-560011, No. 18-52-45023, and No. 19-02-00876 (numerical simulations, magneto-optical measurements); Russian Science Foundation Grant No. 18-12-00475 (numerical simulations). The work was partly supported by the MSU Quantum Technology Center (optical spectroscopy measurements).

-
- [1] W. L. Barnes, A. Dereux, and T. W. Ebbesen, *Nature (London)* **424**, 824 (2003).
- [2] T. W. Ebbesen, C. Genet, and S. I. Bozhevolnyi, *Phys. Today* **61**(5), 44 (2008).
- [3] V. V. Temnov, G. Armelles, U. Woggon, D. Guzatov, A. Cebollada, A. Garcia-Martin, J.-M. Garcia-Martin, T. Thomay, A. Leitenstorfer, and R. Bratschitsch, *Nat. Photon.* **4**, 107 (2010).
- [4] G. Armelles, A. Cebollada, A. García-Martín, and M. U. González, *Adv. Opt. Mater.* **1**, 10 (2013).
- [5] I. Zubritskaya, K. Lodewijks, N. Maccaferri, A. Mekonnen, R. K. Dumas, J. Åkerman, P. Vavassori, and A. Dmitriev, *Nano Lett.* **15**, 3204 (2015).
- [6] A. A. Grunin, A. G. Zhdanov, A. A. Ezhov, E. A. Ganshina, and A. A. Fedyanin, *Appl. Phys. Lett.* **97**, 261908 (2010).
- [7] A. V. Chetvertukhin, A. A. Grunin, A. V. Baryshev, T. V. Dolgova, H. Uchida, M. Inoue, and A. A. Fedyanin, *J. Magn. Magn. Mater.* **324**, 3516 (2012).
- [8] N. Maccaferri, V. A. Inchausti, A. García-Martín, J. C. Cuevas, D. Tripathy, A. O. Adeyeye, and P. Vavassori, *ACS Photon.* **2**, 1769 (2015).
- [9] N. Kostylev, I. S. Maksymov, A. O. Adeyeye, S. Samarin, M. Kostylev, and J. F. Williams, *Appl. Phys. Lett.* **102**, 121907 (2013).
- [10] P. Ferguson, O. Stafsudd, and R. Wallis, *Physica B+C* **86**, 1403 (1977).
- [11] G. S. Krinchik, E. E. Chepurova, and T. I. Kraeva, *Zh. Eksp. Teor. Fiz.* **89**, 277 (1985) [*JETP* **62**, 156 (1985)].
- [12] V. I. Safarov, V. A. Kosobukin, C. Hermann, G. Lampel, J. Peretti, and C. Marliere, *Phys. Rev. Lett.* **73**, 3584 (1994).
- [13] C. Hermann, V. A. Kosobukin, G. Lampel, J. Peretti, V. I. Safarov, and P. Bertrand, *Phys. Rev. B* **64**, 235422 (2001).
- [14] N. Bonod, R. Reinisch, E. Popov, and M. Nevière, *J. Opt. Soc. Am. B* **21**, 791 (2004).
- [15] C. Clavero, K. Yang, J. R. Skuza, and R. A. Lukaszew, *Opt. Lett.* **35**, 1557 (2010).
- [16] G. A. Wurtz, W. Hendren, R. Pollard, R. Atkinson, L. L. Guyader, A. Kirilyuk, T. Rasing, I. I. Smolyaninov, and A. V. Zayats, *New J. Phys.* **10**, 105012 (2008).
- [17] V. I. Belotelov, I. A. Akimov, M. Pohl, V. A. Kotov, S. Kasture, A. S. Vengurlekar, A. V. Gopal, D. R. Yakovlev, A. K. Zvezdin, and M. Bayer, *Nat. Nanotechnol.* **6**, 370 (2011).
- [18] A. V. Chetvertukhin, A. I. Musorin, T. V. Dolgova, H. Uchida, M. Inoue, and A. A. Fedyanin, *J. Magn. Magn. Mater.* **383**, 110 (2015).
- [19] D. Floess, M. Hentschel, T. Weiss, H.-U. Habermeier, J. Jiao, S. G. Tikhodeev, and H. Giessen, *Phys. Rev. X* **7**, 021048 (2017).
- [20] V. G. Kravets, A. V. Kabashin, W. L. Barnes, and A. N. Grigorenko, *Chem. Rev.* **118**, 5912 (2018).
- [21] M. Kataja, T. K. Hakala, A. Julku, M. J. Huttunen, S. van Dijken, and P. Törmä, *Nat. Commun.* **6**, 7072 (2015).
- [22] N. Maccaferri, L. Bergamini, M. Pancaldi, M. K. Schmidt, M. Kataja, S. van Dijken, N. Zabala, J. Aizpurua, and P. Vavassori, *Nano Lett.* **16**, 2533 (2016).
- [23] S. R. K. Rodriguez, A. Abass, B. Maes, O. T. A. Janssen, G. Vecchi, and J. Gómez Rivas, *Phys. Rev. X* **1**, 021019 (2011).
- [24] N. Verellen, P. Van Dorpe, C. Huang, K. Lodewijks, G. A. E. Vandenbosch, L. Lagae, and V. V. Moshchalkov, *Nano Lett.* **11**, 391 (2011).
- [25] Y. Sonnefraud, N. Verellen, H. Sobhani, G. A. Vandenbosch, V. V. Moshchalkov, P. Van Dorpe, P. Nordlander, and S. A. Maier, *ACS Nano* **4**, 1664 (2010).
- [26] W. H. Yang, C. Zhang, S. Sun, J. Jing, Q. Song, and S. Xiao, *Nanoscale* **9**, 8907 (2017).
- [27] T. K. Hakala, H. T. Rekola, A. I. Väkeväinen, J. P. Martikainen, M. Nečada, A. J. Moilanen, and P. Törmä, *Nat. Commun.* **8**, 13687 (2017).
- [28] A. López-Ortega, M. Zapata Herrera, N. Maccaferri, M. Pancaldi, M. Garcia, A. Chuvilin, and P. Vavassori, *arXiv:1903.08392*.
- [29] M.-W. Chu, V. Myroshnychenko, C. H. Chen, J.-P. Deng, C.-Y. Mou, and F. J. García de Abajo, *Nano Lett.* **9**, 399 (2009).
- [30] M. Liu, T.-W. Lee, S. K. Gray, P. Guyot-Sionnest, and M. Pelton, *Phys. Rev. Lett.* **102**, 107401 (2009).
- [31] J. Dorfmueller, R. Vogelgesang, R. T. Weitz, C. Rockstuhl, C. Etrich, T. Pertsch, F. Lederer, and K. Kern, *Nano Lett.* **9**, 2372 (2009).
- [32] A. Y. Frolov, N. Verellen, J. Li, X. Zheng, H. Paddubrouskaya, D. Denkova, M. R. Shcherbakov, G. A. E. Vandenbosch, V. I. Panov, P. Van Dorpe, A. A. Fedyanin, and V. V. Moshchalkov, *Nano Lett.* **17**, 7629 (2017).
- [33] C. Ropers, D. J. Park, G. Stibenz, G. Steinmeyer, J. Kim, D. S. Kim, and C. Lienau, *Phys. Rev. Lett.* **94**, 113901 (2005).
- [34] Y. Hua, A. K. Fumani, and T. W. Odom, *ACS Photon.* **6**, 322 (2019).
- [35] G. Vecchi, V. Giannini, and J. Gómez Rivas, *Phys. Rev. B* **80**, 201401(R) (2009).

- [36] D. Regatos, D. Fariña, A. Calle, A. Cebollada, B. Sepúlveda, G. Armelles, and L. M. Lechuga, *J. Appl. Phys.* **108**, 054502 (2010).
- [37] A. A. Grunin, I. R. Mukha, A. V. Chetvertukhin, and A. A. Fedyanin, *J. Magn. Magn. Mater.* **415**, 72 (2016).
- [38] D. Martín-Becerra, J. B. González-Díaz, V. V. Temnov, A. Cebollada, G. Armelles, T. Thomay, A. Leitenstorfer, R. Bratschitsch, A. García-Martín, and M. U. González, *Appl. Phys. Lett.* **97**, 183114 (2010).
- [39] M. G. Barsukova, A. S. Shorokhov, A. I. Musorin, D. N. Neshev, Y. S. Kivshar, and A. A. Fedyanin, *ACS Photon.* **4**, 2390 (2017).
- [40] I. S. Maksymov, *Rev. Phys.* **1**, 36 (2016).
- [41] M. G. Barsukova, A. I. Musorin, A. S. Shorokhov, and A. A. Fedyanin, *APL Photon.* **4**, 016102 (2019).
- [42] P. P. Vabishchevich, A. Y. Frolov, M. R. Shcherbakov, A. A. Grunin, T. V. Dolgova, and A. A. Fedyanin, *J. Appl. Phys.* **113**, 17A947 (2013).
- [43] M. R. Shcherbakov, P. P. Vabishchevich, A. Y. Frolov, T. V. Dolgova, and A. A. Fedyanin, *Phys. Rev. B* **90**, 201405(R) (2014).
- [44] V. V. Temnov, *Nat. Photon.* **6**, 872 (2012).
- [45] D. Bossini, V. I. Belotelov, A. K. Zvezdin, A. N. Kalish, and A. V. Kimel, *ACS Photon.* **3**, 1385 (2016).
- [46] See Supplemental Material at <http://link.aps.org/supplemental/10.1103/PhysRevB.101.045409> for details of (1) the simulations of the extinction cross section of the individual Au/Ni/Au nanowire; (2) phase of electric field of localized surface plasmon, bright and dark modes in MPCs; (3) comparison of SPP and SLM wavelength.
- [47] Lumerical FDTD Solutions, <http://www.lumerical.com>.